SIMULATION OF MICROPOROSITY IN ALUMINUM PLATE CASTINGS

By

Enrique Escobar de Obaldia

A Thesis
Submitted to the Faculty of
Mississippi State University
in Partial Fulfillment of the Requirements
for the Degree of Master of Science
in Mechanical Engineering
in the Department of Mechanical Engineering

Mississippi State University

May 2007

SIMULATION OF MICROPOROSITY IN ALUMINUM PLATE CASTINGS

By

Enrique Escobar de Obaldia

Approved:

Sergio D. Felicelli Associate Professor of Mechanical Engineering (Major Professor)	Mark F. Horstemeyer Center for Advanced Vehicular Systems Chair in Computational Solid Mechanics Professor of Mechanical Engineering (Committee Member)
John T. Berry E. P. Coleman Professor of Mechanical Engineering (Committee Member)	W. Glenn Steele Professor of Mechanical Engineering and Department Head
Steven R. Daniewicz Professor and Graduate Coordinator Department of Mechanical Engineering	W. Glenn Steele Dean of the College of Engineering

Name: Enrique Escobar de Obaldia

Date of Degree: May 4th, 2007

Institution: Mississippi State University

Major Field: Mechanical Engineering

Major Professor: Dr. Sergio D. Felicelli

Title: SIMULATION OF MICROPOROSITY IN ALUMINUM PLATE CASTINGS

Pages in Study: 48

Candidate for Degree of Master of Science

Porosity is known to be one of the primary factors controlling fatigue life and total elongation in cast aluminum components. The thrust of this study is to examine pore nucleation and growth effects for predicting gas microporosity in A356 plates. In this work, a solidification model is used to quantify and evaluate the discrepancy between experimental data and porosity calculated with different approaches. The first approach considers hydrogen supersaturation based on the transport of dissolved hydrogen and Sievert's law. The second approach uses the hydrogen supersaturation calculated in the first approach combined with a local solidification time. The third approach considers a new hydrogen technique based on the transport of inclusions through the liquid metal and mushy zone. Computer simulations were performed modeling aluminum plate castings.

DEDICATION

This is dedicated to my father, mother and sister. Also to my grandmother who died during my first year of graduate school.

ACKNOWLEDGMENTS

I would like to give my sincere gratitude to the people who helped make this Master's Thesis possible. First, I would like to give the thanks to Dr. Sergio Felicelli for his guidance, teaching and patient in these years of master's degree. I would also like to give the thanks to Dr. Mark Horstemeyer for helping me to come to Mississippi State University and for encouraging me to continue my education after my bachelor degree. Thanks also to Dr. John Berry for contributing to my academic development. Finally, I want to give the thanks to the people that work at the Center for Advanced Vehicular Systems for always been there anytime that I needed them and to the National Science Foundation through Grant Number CTS-0553570 that partly funded this research.

TABLE OF CONTENTS

LIST OF TABLES

LIST OF FIGURES

CHAPTER I

INTRODUCTION

1.1 Overview

Over the last few decades, the automotive industry has been seeking to improve the performance of vehicles, and one particular way can be by reducing the weight of individual components. Aluminum castings have been a great solution to reduce weight and enhance the mechanical properties of the automobile's parts. However, their application has been limited by the variable properties that aluminum castings have shown sometimes in material tests. These properties have been attributed to the combination of defects during the solidification process: coarse intermetallic phase particles, oxide films, inclusions, non uniform microstructure and porosity.

This last defect, porosity, can be classified by the size or by the origin within the castings. Macroporosity and microporosity are the pore size classifications. Microporosity refers to pores which range in size from micrometers to hundreds of micrometers and usually to occupy the interdendritic spaces near the end of solidification. The porosity can be due to shrinkage that is created by the volume difference between the solid and liquid phases of a metal or due to gas porosity that is the presence of dissolved gas elements in the liquid

alloys or a combination of both. The shrinkage porosity can have the form of a large void or distributed small pores, whereas gas porosity is observed normally as small distributed pores. Gas porosity is produced when an excess of hydrogen in the form of bubbles is not incorporated in the liquid or solid-liquid area [1]. In the case of aluminum alloys, hydrogen is the most active gaseous element leading to gas porosity [2]. Porosity is known to be one of the primary factors controlling fatigue lifetime and total elongation in cast aluminum components. Therefore, feeding systems for castings must be designed to allow the minimum porosity formation. One fast and inexpensive solution for feeding design is computer solidification modeling.

The computer simulations will provide knowledge about the conditions necessary to avoid pore formation. In that way many simulations can be performed in short times just to design one feeding system. Nucleation, that is the formation of one phase from another phase, is one of the most challenging mechanisms that can be modeled with computer simulations. To conclude this introduction the bifilms definition should be explained, the bifilms theory has been introduced and developed in grand part by John Campbell [1]. The bifilms is the enfolding of the liquid surface into the bulk metal and because the surface usually has a film that is folded double hence the name “bifilms”.

Many efforts have been devoted to the modeling of porosity formation in the last 20 years, particularly in aluminum [3-8] and, in lesser degree, nickel superalloys [1,9] and steels [10,11]. More recently, rather sophisticated models have been developed to include the effects of pores on fluid flow (three-phase

transport) [12], multiscale frameworks that consider the impingement of pores on the microstructure [13], and new nucleation mechanisms based on entrainment of oxide bifilms [14]. A recent review on the subject of computer simulation of porosity and shrinkage related defects has been published by Stefanescu [15].

1.2 Objectives of study

This study comprises three objectives. The first objective is to extend the solidification capabilities of MULTIA [16], in order to acquire a better understanding of microporosity formation in A356 aluminum alloy castings. The second objective is to apply three calculation methods with different implications and assumptions to predict the amount of porosity in aluminum alloy castings. Finally, the last goal of this research is to compare the results obtained with the methods to experimental data. The pore volume fraction and the pore size distribution are some of the constants obtained in this study.

The results presented in this thesis have been published in three journal articles [17, 18, and 19] and presented in several scientific conferences [20, 21, and 22].

CHAPTER II

BACKGROUND OF MODELING WORKS FOR ALUMINUM ALLOYS

The pioneering studies in microporosity prediction in metal alloy castings were begun in the 1960's by Flemings and colleagues [23, 24, 25, and 26]. Some remarks of these works are the consideration of interdendritic flow through a fixed dendritic solid, the development of the local solute redistribution equation and the use of Darcy's law for flow in porous media. Today's solidification models still use many of the innovative aspects introduced by Flemings and coworkers.

In the last three decades, well developed studies, inspired by the early works of Flemings and coworkers, appeared in scientific publications. Newer models derived from these studies differ from the models presented in the 60's and 70's in that they address a set of momentum, energy and mass transport equations equally valid for the liquid, solid and solid-liquid area. Hence, the new models require computer systems with the latest technologies that have been developed over those years. Fang and Granger [3] presented, in 1989, a three stage hydrogen porosity model based on a temperature dependence of liquid, eutectic and solid phase. The mathematical model considers a threshold cell radius of concentric spheres for pore formation. In this work, the effects of hydrogen content and local solidification characteristics (grain size and/or

dendrite cell size) are studied to predict the growth of pores during the solidification of A356 alloy castings. Experiments also were performed to define quantitatively the effects of hydrogen content, solidification conditions and grain refining on pore morphology, using a directional solidification setup. A further explanation of this experimental methodology will be given during this paper.

A study presented by Taylor et al. [27] examines the role of the permeability calculations in the mushy zone for an A356 aluminum alloy. The criteria functions studied are a combination of casting thermal and material parameters; and were derived from one-dimensional continuity and momentum flow equations. One remarkable conclusion of the authors is that the criteria functions studied did not account in the evolution of dissolved gasses. Also, they suggest the incorporation of oxide films for porosity formation, which has been developed for many years by John Campbell [1].

A complete study in hydrogen porosity was presented by Lee and Hunt [5] in 2001. A stochastic model of diffusion controlled porosity growth was presented by the authors. The mathematical model was used to describe the experimental results obtained with the X-ray Temperature Gradient Stage (XTGS). The XTGS was used for *in-situ* observations and incorporated a stochastic mechanism of pore nucleation, solute partitioning and primary dendrite arm spacing [28]. The mathematical formulation neglects buoyancy and shrinkage effects in the two dimensional model. The model employs an initial and limited radius values; this last one is imposed once the pore impinges on the microstructure. The ideal gas law, Scheil equation and law of mixtures are some

of the expressions used to calculate the final diameter of the pores. The potential site criteria necessary to activate the future pores was generated with the experimental data of the XTGS observations. An innovative aspect of this study was that each individual pore was tracked during the solidification time. The importance of the hydrogen diffusion and the effects of the solidification velocity were summarized in the final conclusions of this work.

Using a finite element model for simulating dendritic solidification, Poirier et al. [7] calculated the pressure and redistribution of hydrogen during solidification of A356 aluminum castings in 2001 using the model by Felicelli et al [2]. A two-phase microporosity model (liquid and solid) solves the continuity, energy, momentum and solute conservation equations. The model allows for the consideration of different solutes in the calculations. The porosity condition for this model is determined by the liquid pressure (pressure outside the pore) and the gas pressure (calculated with the Sievert's expression). The model assumes that the pores have a radius larger than 20 μm and, in that way, neglects the surface tension for the porosity formation condition. The model concluded that pore formation is less sensitive to the grain size than to the initial hydrogen concentration. One important contribution of this paper is the figures showing the distribution of hydrogen and gas pressure in a plate casting.

Han and Viswanathan [4] studied hydrogen concentration during directional solidification of an Al – 4.5% Cu alloy. They emphasized the predictions made when applying the lever rule for calculating the hydrogen concentration in the liquid. A one dimensional model, assuming no diffusion, is

considered in this work. An experimental setup using cooled plate casting of Al – 7% Si and thermocouples was presented by M'Hamdi et al. [6] in 2003. The results of these feeding experiments were modeled using CALCOSOFT. In a two dimensional domain, where shrinkage porosity and microsegregation of hydrogen are taken into account, M'Hamdi et al. show the importance of mobility limit and gas content on the final amount of porosity.

In 2005, Zhu et al. [8] presented a numerical model for predicting microporosity formation in aluminum alloy castings. A series of experimental tests were carried out on A356 alloy castings using directional solidification processes; the results obtained were used to validate the model predictions. The hydrogen content, porosity amount and pore size were some of the variables studied in the experiments. The mathematical formulation module was based on Darcy flow and hydrogen redistribution, and implemented into the ABAQUS commercial package. The conservation equations of mass and momentum were solved to calculate the pressure and velocity fields. A two-stage approach was used in the porosity prediction where, for low initial hydrogen contents, only the Niyama criterion [29] determines porosity formation. An initial threshold hydrogen content of 0.05 cc/100g for pore formation was found in this study.

CHAPTER III

SOLIDIFICATION MODEL

3.1. Overview

The model presented here is built upon the robust and well-tested multicomponent solidification model MULTIA, which calculates macrosegregation during solidification of a dendritic alloy with many solutes [30]. MULTIA solves the conservation equations of mass, momentum, and energy, for each alloy component within a continuum framework in which the mushy zone is treated as a porous medium of variable permeability. In order to predict whether microporosity forms, the solidification shrinkage due to different phase densities, the concentration of gas-forming elements and their redistribution by transport during solidification were added to the model later [2]. In this form, MULTIA was able to predict regions of porosity formation by comparing the Sievert's pressure with the local pressure. The model has already been presented in detail [2, 11] and only the main assumptions and governing equations are presented here.

3.2 Conservation equations

The following assumptions are invoked: the liquid is Newtonian and the flow is laminar; the Boussinesq approximation is made in the buoyancy term of

the momentum equation; the solid phase is stationary; the gas phase does not affect the transport equations (two-phase model); and the densities of solid (ρ_s) and liquid (ρ_l) are different but constant. With these assumptions, the conservation equations can be written as:

Mass and momentum:

$$\nabla \cdot \mathbf{u} = \beta \frac{\partial g_l}{\partial t} \tag{1}$$

$$g_l \frac{\partial}{\partial t}\left(\frac{\mathbf{u}}{g_l}\right) + \mathbf{u} \cdot \nabla\left(\frac{\mathbf{u}}{g_l}\right) = -\frac{g_l}{\rho_l}\nabla p + \frac{\mu}{\rho_l}\nabla^2 \mathbf{u} - \frac{\mu}{\rho_l}\frac{g_l}{\mathbf{K}}\mathbf{u} + \frac{\mu\beta}{3\rho_l}\nabla\left(\frac{\partial g_l}{\partial t}\right) + \frac{\rho g_l}{\rho_l}\mathbf{g} \tag{2}$$

Energy:

$$\overline{\rho c}\frac{\partial T}{\partial t} + \rho_l c_l \mathbf{u} \cdot \nabla T = \nabla \cdot \bar{\kappa}\nabla T - \rho_s\left[L + (c_l - c_s)(T - T^H)\right]\frac{\partial g_l}{\partial t} \tag{3}$$

Solutes:

$$\frac{\partial \overline{\rho C}}{\partial t} + \rho_l \mathbf{u} \cdot \nabla C_l = \nabla \cdot \overline{\rho D \nabla C} - \beta \rho_l \frac{\partial g_l}{\partial t} C_l \tag{4}$$

In the above equations, u is the superficial velocity, g_l is the volume fraction of liquid, t is time, ρ is density, β is the shrinkage coefficient $\beta = (\rho_s - \rho_l)/\rho_l$, p is pressure, μ is viscosity, g is gravity, K is the permeability, T is temperature, c is specific heat, κ is the thermal conductivity, L is latent heat, T^H is a reference temperature, C is the solute concentration in weight per cent, and D is solute diffusivity. The subscripts *"s"* and "*l*" refer to solid and liquid, respectively, while a bar over a variable means a volume average of the variable over the solid-liquid mixture; for example, $\bar{\rho} = g_l\rho_l + g_s\rho_s$,

where g_s is the volume fraction of solid. Several equations (4) are solved in the model, one per each solute. The energy and solute-equations are rearranged in modified form, depending whether the solute is assumed to have negligible or complete diffusion in the local solid (like hydrogen).

The body force term (*i.e.*, the last term on the right side of Equation (2)) assumes the Boussinesq approximation, in which the density of the liquid, ρ varies with temperature (T) and solute concentrations (C) from its reference value, ρ_l, according to

$$\rho = \rho_l \left[1 + \beta_T \left(T - T_R\right) + \sum_{j=1}^{N} \beta_C^j \left(C_l^j - C_R^j\right) \right] \tag{5}$$

where $\beta_T = (1/\rho_l)\,(\partial\rho/\partial T)$ is the thermal expansion coefficient, $\beta_C^j = (1/\rho_l)\,(\partial\rho/\partial C_l^j)$ are the solutal expansion coefficients, N is the number of alloy elements, and the superscript j refers to a particular solute or alloy element. The reference density is the density of the liquid at the reference temperature, T_R, and the reference composition ($C_R^1, C_R^2, C_R^3, ... C_R^N$).

The liquidus temperature of the liquid, T_L, in the mushy zone is a function of the local composition (no undercooling of the intergranular liquid is allowed). Hence,

$$T_L = T_o + \sum_{j=1}^{N} m^j\, C_l^j \tag{6}$$

where the value of m^j is a constant (or function) unique to the alloy element j, and T_o is the melting temperature of the pure solvent.

For the equiaxed microstructures simulated in this work, the permeability is assumed isotropic, and is based on empirical data of permeabilities and numerical simulations of flows through microstructures of partially solidified and quenched alloys [31]. The microstructure length scale is taken as the inverse of the specific area of a grain, S_V^{-1}, which can be written in terms of the volume fraction solid as [2]:

$$S_V^{-1} = \omega \left(\frac{3 g_s}{4\pi} \right)^{1/3} d \tag{7}$$

where *d* is the final grain diameter and ω is a shape parameter of the grain.

The reader is referred to Felicelli *et al* [2] or Sung *et al* [11] for more specific details on the model regarding additional rearrangement of equations and numerical solution procedures.

3.3 Thermodynamics of hydrogen in A356

The solubility of gas-elements decreases with decreasing temperature, and there is a large reduction in solubility during solidification. Gas-forming elements dissolved in cast metals partition to the intergranular liquid and can precipitate as a gas. Hydrogen is the most common of the gas-forming elements, and it dissolves atomically in both the liquid and the solid according to the following reaction:

$$\tfrac{1}{2} \mathrm{H}_2 (g) = \underline{\mathrm{H}} \tag{8}$$

where $H_2(g)$ represents the gas phase and $\underline{H}$ is the hydrogen dissolved in the liquid metal. The pressure of hydrogen gas, which is in equilibrium with liquid metal having a dissolved hydrogen concentration, C_H (wt pct), is given by Sievert's law [26]:

$$K_H = \frac{C_H f_H}{(P_{H_2})^{1/2}} \tag{9}$$

where P_{H_2} is the pressure of hydrogen gas in atm, and K_H and f_H are the equilibrium constant and activity coefficient, respectively, for hydrogen. The activity coefficient for hydrogen in A356 [32-34] is estimated as:

$$\ln f_H = \sum_{j=1}^{N} a_H^j C^j + \sum_{j=1}^{N} b_H^j (C^j)^2 \tag{10}$$

where a_H^j and b_H^j are interaction coefficients and C^j is the concentration of solute element *j*. Using Equations (9) and (10) with values of the interaction coefficients, the Sievert's gas pressure of hydrogen or, equivalently, the solubility of hydrogen at a given liquid pressure, can be calculated.

CHAPTER IV

EXPERIMENTAL SETUP

The experimental results, used to compare the certainty of the modeling predictions proposed in this thesis, were obtained by Fang and Granger [3]. The thermal boundary conditions of a unidirectional solidification casting were extracted from this experimental setup and used to compare the model capabilities. In these experiments, Pyrotec R2020, a refractory material of low thermal mass ,was used for the mold's walls. A 2.6 cm x 8 cm x 30 cm mold was used as shown in Figure 4.1. The mold contains a copper plate at the bottom that, after filling with the aluminum melt and establishing a solid shell (20 seconds after start the process), will be withdrawn to allow cooling water to impinge directly on the solidifying casting at a flow rate of 9.5 liters/min. The molds were preheated to approximately 700 C in a separate furnace. In order to have a unidirectional solidification casting, both the mold and melt should be preheated at a temperature above the liquidus before starting the process.

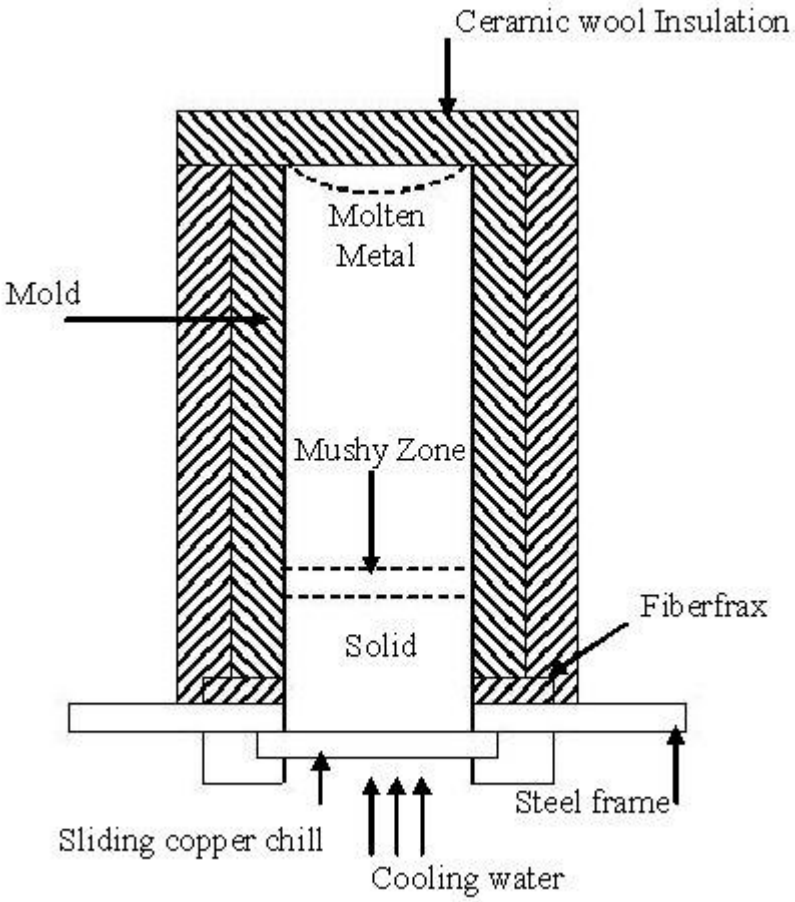

Figure 4.1 Scheme of experimental setup for a unidirectional solidification casting [3]

The study performed by Fang and Granger [3] considered initial hydrogen contents of 0.11 cc/100g, 0.25 cc/100g and 0.31 cc/100g with grain refiner addition (TiB) and one case of strontium modification. The castings obtained (about 28 cm long) were cut into pieces for various analyses including chemistry, hydrogen content determination, optical metallography and dry checking, were done to obtain grain morphology, pore volume evolution, pore volume fraction and pore size distribution measurements using the LeMont SEM technique.

The thermodynamic and transport properties of the alloy used in the simulations, including the alloy elements and hydrogen, are the same as the ones in Poirier et. al [7], with the exception of the hydrogen partition coefficient, for which the developments of Poirier and Sung [34] were used to include the effect of the high eutectic fraction in A356 (Table 5.1).

Table 4.1.

A356 properties

Element	Al	Si	Mg	*H*
Alloy Composition (wt%)	Base Element	7.0	0.3	*0.07*
Equilibrium Partition Ratio	Base Element	0.131	0.426	0.04 ($T>T_E$), 0.28 ($T=T_E$)

CHAPTER V

MODELING METHODS

The modeling methods presented here were added to the solidification code MULTIA. As mentioned in Chapter III, the model lacked the capability of calculating the amount of porosity and size of pores. The porosity extension added by this work includes the calculation of an initial approximation to the amount of porosity assuming supersaturation, a proposed correction for the supersaturation overpredictions based in modeling and experimental data, and finally, a more developed and justified hydrogen diffusion method based on an initial pore radius and inclusions number.

5.1. Method A – Hydrogen supersaturation technique

5.1.1 Condition for porosity formation

A gas element dissolved in a liquid alloy forms micropores when its equilibrium, Sievert's pressure, exceeds the local pressure within the intergranular liquid plus the excess pressure attributed to surface tension. A pore exists and is capable of growing provided that:

$$P_G > P + \frac{2\sigma_{GL}}{r} \quad (11)$$

where P_G is the Sievert's gas pressure (*i.e.*, the hydrogen pressure within the pore) and P is the local pressure in the intergranular liquid. The local pressure is the sum of the ambient pressure, the metallostatic pressure, and the pressure drop due to friction that develops when the intergranular liquid flows to "feed" the shrinkage. The term, $2\sigma_{GL}/r$, is an added pressure, due to surface tension of a pore with a radius of curvature r. For pores larger than about r = 20 μm, the surface-energy term on the right side of Equation (11) is less than 1 atm, and the effects of surface tension are not considered for these calculations. By ignoring the effects of surface tension, predictions of the volume fraction of porosity are overestimates.

5.1.2 Calculation of the volume fraction of gas porosity

The calculation of the volume fraction of hydrogen microporosity is based on the method of Poirier *et al*. [35], in which the mass of gas is assumed to be given by the supersaturation of hydrogen in both the liquid and the solid phases:

$$100m_H = \left(C_l^H - S_l^H\right)g_l + \left(C_s^H - S_s^H\right)g_s \quad (12)$$

where m_H is the mass fraction of hydrogen, C_l^H and C_s^H are the concentrations of hydrogen in wt %, and S_l^H and S_s^H are the solubilities. Equation (12) assumes that all of the hydrogen exceeding the solubility will become gas pores, which is

of course an overestimation that ignores the nucleation barriers. The solubility of hydrogen in the liquid is calculated with the Sievert's law, Equation (9), while for the solid it can be take $S_s^H = k_H S_l^H$, where k_H is the partition coefficient of hydrogen. Also, complete diffusion of hydrogen is assumed in the local solid, hence $C_s^H = k_H C_l^H$, and Equation (12) can be rewritten as:

$$100 m_H = \left(C_l^H - S_l^H\right)\left(g_l + k_H g_s\right) \tag{13}$$

Assuming ideal gas behavior, it can then calculate the volume fraction of hydrogen as:

$$g_H = \frac{m_H \bar{\rho} RT}{M P_{H_2}} \tag{14}$$

where R is the gas constant, M is the molecular weight of hydrogen gas and $\bar{\rho}$ is the density of the solid-liquid mixture.

5.2. Method B – Semi-Empirical technique

The problem with the above approach is that Equation (12), from which Equation (14) is derived, assumes that all of the hydrogen exceeding the solubility will become gas pores, which of course is an overestimation because the pores need to overcome nucleation barriers in order to become actual pores. Most of the mechanisms that have been proposed for the nucleation of pores are based on the size of interdendritic cavities and the theory of heterogeneous

nucleation on non-wetted surfaces. After nucleation, pore growth occurs by diffusion of hydrogen into the pore. These ideas have been challenged by John Campbell [14] and others, who propose a nucleation-free mechanism for pore formation, based on the concept of double oxide films or bifilms. In this scenario, during pouring in a casting process, the liquid surface of the alloy can fold upon itself. Because the liquid surface is covered by an oxide film, the folding action leads to bifilms, which are entrained into the bulk melt as a pocket of air enclosed by the bifilm. In effect, the bifilms, with its air pocket, is the beginning of a pore. After entrainment, the turbulence causes the bifilm to convolute and contract. Posterior pore growth can occur by the simple action of unfurling of the bifilms, without the aid of hydrogen diffusion.

Although the identification of the mechanisms of pore formation and growth is still a subject of active research, the following two observations are supported by a large number of experimental and modeling works with aluminum alloys:

a) The amount of porosity increases for higher initial hydrogen content in the alloy.

b) The amount of porosity decreases for higher cooling rate.

In view of these observations, it is proposed to modify the calculated volume fraction of porosity given by Equation (14) according to:

$$g_P = a g_H t_f^b + g_k \tag{15}$$

where g_P is the corrected volume fraction of porosity, g_H is the volume fraction of hydrogen porosity assuming complete precipitation of the supersaturation (calculated in Equation (14)), t_f is the local solidification time (calculated from the solidification history), *a* and *b* are experimental constants, and g_k is the volume fraction of porosity due to interdendritic shrinkage. In most cases with non-negligible hydrogen content, this last term is small compared with gas porosity; shrinkage porosity will not be considered in this work. Note that in Equation (15), g_H is implicitly also a function of the freezing time through the convection and segregation that occurred during solidification. The constant *a,* in Equation (15), is linked to the origin mechanism of the pores. From the heterogeneous nucleation perspective, it can be viewed as the fraction of inclusions or sites that overcame the nucleation barriers in a H-supersaturated environment; from the double oxide bifilm perspective, it can be viewed as the fraction of bifilms that became active by the unfurling mechanism. The constant *b,* in Equation (15), is linked to the pore growth mechanism and carries information about the time that the pores need to grow by hydrogen diffusion and/or unfurling. A relation similar to Equation (15), but without the supersaturation and shrinkage terms, was used by Anyalebechi [36] to analyze experimental results with alloy A356.

5.3. Method C – Hydrogen diffusion technique

In the hydrogen diffusion technique, a pore growth model is implemented at the microscopic scale together with a criterion for nucleation of pores. The term nucleation is used here in the general sense to refer to the origination of pores, without necessarily implying any particular mechanism of classical nucleation. It is assumed that, dispersed in the liquid, there is an initially known distribution of microscopic inclusions. These can be oxide bifilms that were entrained during melt pouring, old oxide bifilms that existed in the melt before pouring, or other impurities that serve as possible nucleation sites for hydrogen pores. We call $n(\mathbf{x},t)$ the number of these inclusions per unit volume of alloy, where $n(\mathbf{x},0)$ is known. The inclusions are transported with the velocity field, u, of the liquid and they can partition to the solid like the other solutes of the alloy. For implementation purposes, the inclusions are treated as another alloy solute with negligible diffusion.

5.3.1 Condition for porosity formation

It is assumed that hydrogen pores can nucleate and grow only at places where the following two conditions are met:

$$n(x,0) > 0 \quad \text{and} \quad p_S > p + \frac{2\sigma}{r} \tag{16}$$

where p is the pressure of the liquid and p_S is the Sievert pressure given by Equation 9. When conditions (16) are met, it is assumed that a concentration n

of spherical pores form with a known average initial radius, r_0. If the pores are in a supersaturated environment, they will grow by hydrogen diffusion.

5.3.2 Porosity modeling

Assuming that the pores maintain the spherical shape during growth in the liquid, the mass rate of hydrogen entering the pore by diffusion from the liquid is given by:

$$\frac{dm^H}{dt} = 4\pi r_P^2 \rho_l D_H \left.\frac{\partial C_l^H}{\partial r}\right|_{r=r_P} \tag{17}$$

Where r_P is the pore radius, r is the radial coordinate measured from the center of the pore, and D_H is the diffusivity of hydrogen in the liquid. It is assumed that the hydrogen gas inside the pore behaves as an ideal gas and that the partial pressure of other gases in the pore is negligible compared to that of hydrogen (this is reasonable in Al alloys given the high diffusivity of H compared to other gases). In this case, the rate of increase of the volume of the pore can be calculated as:

$$\frac{dV_P}{dt} = \frac{R_H T}{p_S}\frac{dm^H}{dt} \tag{18}$$

where R_H is the hydrogen gas constant. The radius of the pore is then obtained as:

$$r_P = \left(\frac{3}{4\pi} V_P \right)^{1/3} \tag{19}$$

To estimate the radial derivative in Equation (17), we follow Yin and Koster [36] and consider the thickness of the diffusion boundary layer around the pore:

$$\left. \frac{\partial C_l^H}{\partial r} \right|_{r=r_P} \cong \frac{C_l^H - C_P}{\delta} \quad ; \quad \delta = 4\sqrt{D_H t} \tag{20}$$

where C_P is the concentration of hydrogen at the pore surface, given by Equation (9), and t is the time measured since pore nucleation. We must keep in mind that the pore growth model exists at the microscopic scale; there are no actual pores that are part of the geometry of the macroscopic model (the radial direction has no meaning in the macroscopic model). The pore radius calculated in Equation (19) should be interpreted as the average radius of pores in a location x where there are $n(x, t)$ pores per unit volume.

Equation (17) is valid for pores that grow in the liquid. For pores growing in the mushy zone, the diffusion flux is taken as an average for liquid and solid [7] and the pore area is multiplied by a shape parameter, α, in order to account for the distortion of the pores as they impinge into dendrites, with:

$$\alpha = \frac{r_P S_V}{3} \tag{21}$$

where α is the pore shape parameter and S_V is the specific area of the pore (ratio of pore area to pore volume). For spherical pores, $\alpha = 1$, while $\alpha > 1$ for pores distorted by dendrites.

The pores grow while there is liquid remaining around them and lock in size after complete solidification. The total fraction of porosity in the casting as a function of time can be calculated as:

$$f_P(t) = \frac{1}{V}\int_V n(\mathbf{x},t)V_P(\mathbf{x},t)d\mathbf{x} \tag{22}$$

where V is the volume of the casting.

To close the model, it is needed to provide some mechanism by which the concentration of dissolved hydrogen in the bulk liquid around the pore decreases to compensate the hydrogen provided to the pore (otherwise the pore will continue to grow indefinitely). That is, the transport equation for hydrogen needs to be modified to include a sink term. In the liquid, this equation is:

$$\frac{\partial C_l^H}{\partial t} = D_H \nabla^2 C_l^H - \mathbf{u}\cdot\nabla C_l^H - nC_l^H \frac{dV_P}{dt} \tag{23}$$

where the last term in the right hand side represents the amount of hydrogen entering the pores from the liquid by diffusion. Because MULTIA is a two-phase code (liquid and solid), the gas phase is not included in the transport equations. Therefore, the validity of the proposed model needs to be restricted to small volume fraction of porosity, which is reasonable for the usual level of hydrogen

microporosity measured in aluminum castings, (< 1%). In this case, we can assume that the presence of the pores does not affect the transport of other quantities like energy and momentum considerably.

CHAPTER VI

RESULTS AND DISCUSSIONS

The solidification model is discretized in space and integrated in time using a finite element algorithm that is described by Felicelli *et al.* [2, 16]. Aluminum A356 alloy is solidified during this simulation in a bottom-cooled two-dimensional mold. The two-dimensional simulated casting has dimensions of 26 mm in width and 300 mm in height. In addition to the alloy solutes in A356 (Si and Mg), the gas-forming element, hydrogen, is considered. The computational domain is the casting; the top boundary is left open, to allow liquid flow to feed shrinkage. A no-slip condition is used for velocity at the bottom and two vertical boundaries, and a stress-free condition is used on the top open boundary. Solute diffusion flux is set to zero at the boundaries, with the exception of hydrogen, for which a dehydrogenation flux condition is used.

In Figure 6.1, the iso-contour plots of temperature, volume fraction of liquid and total concentration of hydrogen after 400s of simulation time, are illustrated. These results were calculated with the original program of MULTIA before the addition of the porosity extension. At 400s of solidification time, approximately half of the casting has solidified completely and the mushy zone

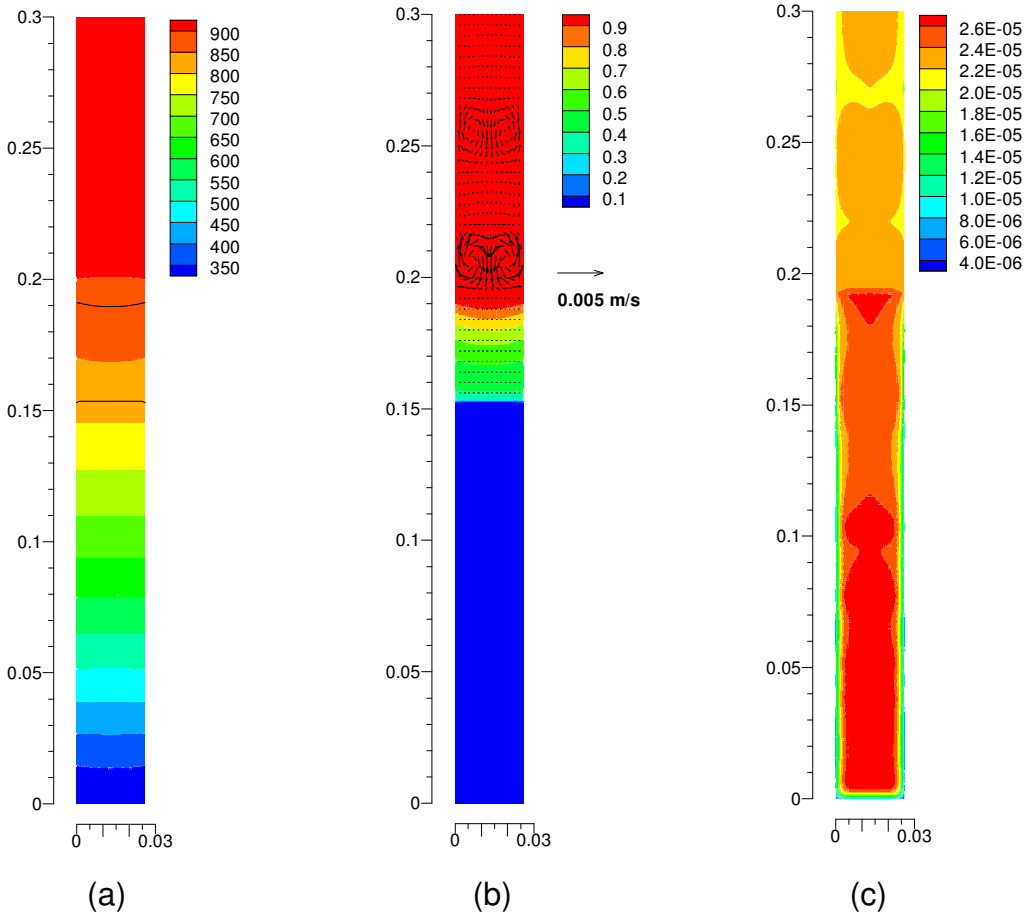

Figure 6.1 Solidification of A356 plate casting at 400 s for 0.31 cc/100g of hydrogen content. (a) isotherms in K; (b) volume fraction of liquid and velocity vectors; (c) total concentration of H in wt%.

(solid-liquid area) is about 40 mm thick. Lines were drawn in Figure 6.1 (a) to indicate the liquidus (bottom line) and eutectic (top line) isotherms. In the top 10% of the mushy zone, the velocities reduce to less than 10^{-6} m/s and their effects in the pressure and other parameters will be neglected in the calculations.

6.1. Method A – Hydrogen supersaturation technique

6.1.1 Effect of initial hydrogen content

The effects of the initial hydrogen content on gas microporosity are analyzed. Figure 6.2 shows the calculated pore volume fraction as a function of the cooling rate. It is observed that the amount of porosity increases for higher initial hydrogen content. This trend is in agreement with the experimental data of Fang and Granger [3]. However, the calculated amount of porosity is much larger than the experimental data. For example, for 0.31 cc/100g of hydrogen content, Fang and Granger [3] reported a measured range of the volume fraction of porosity between 0.03 and 0.7%, while the range obtained in the simulations is 1.16 to 1.57%.

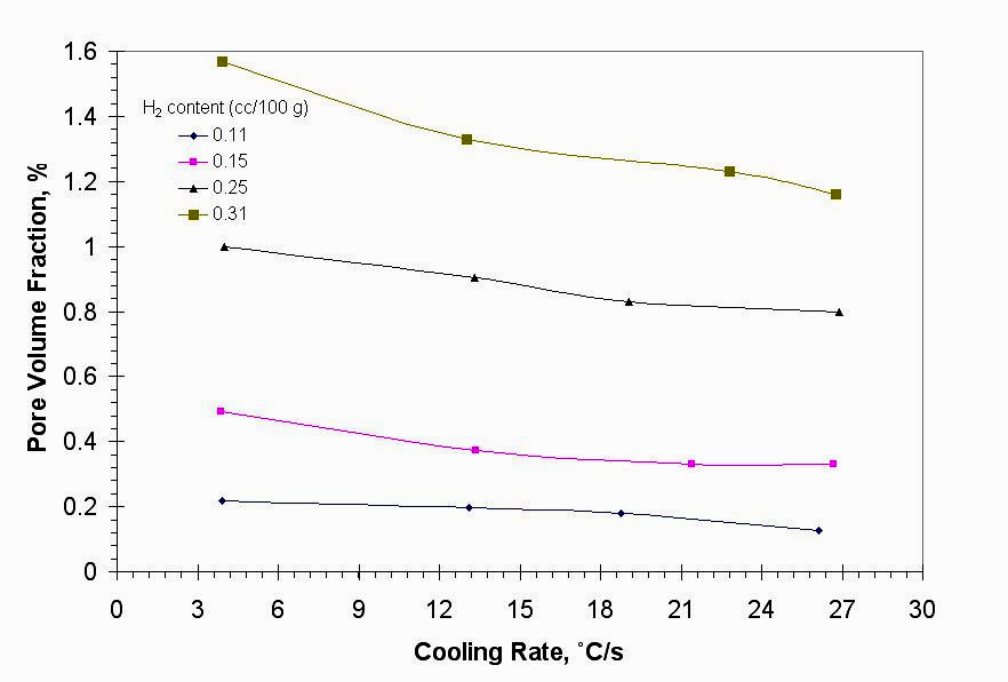

Figure 6.2 Volume fraction of porosity for different initial hydrogen content as a function of cooling rate

The discrepancy between the experimental data is expected because, in Equation (12), it is assumed that all of the hydrogen supersaturation goes to the pores. Neglecting the nucleation and growth effects resulted in the discrepancy between the trends of cooling rate for predicted and experimental values.

6.1.2 Effect of cooling rate

The potential volume fraction of porosity, as a function of hydrogen content, is shown in Figure 6.3. It is observed that the amount of porosity due to cooling rate increases when we increase the hydrogen content. This trend is seen also in the experimental data, but with a higher slope of growth, indicating that, in our modeling, the nucleation and growth effects are more active at large supersaturations. In comparing the simulation results with the experiments, it is assumed implicitly that most of the measured porosity was hydrogen-induced and that the amount of shrinkage porosity is small. This seems to be confirmed by Fang and Granger [3], who observed, in SEM images, quite spherical pores surrounded by eutectic phase. The high fraction of eutectic phase ensures that pores are surrounded mostly by liquid throughout solidification, promoting the unconstrained growth of spherical gas pores by hydrogen diffusion.

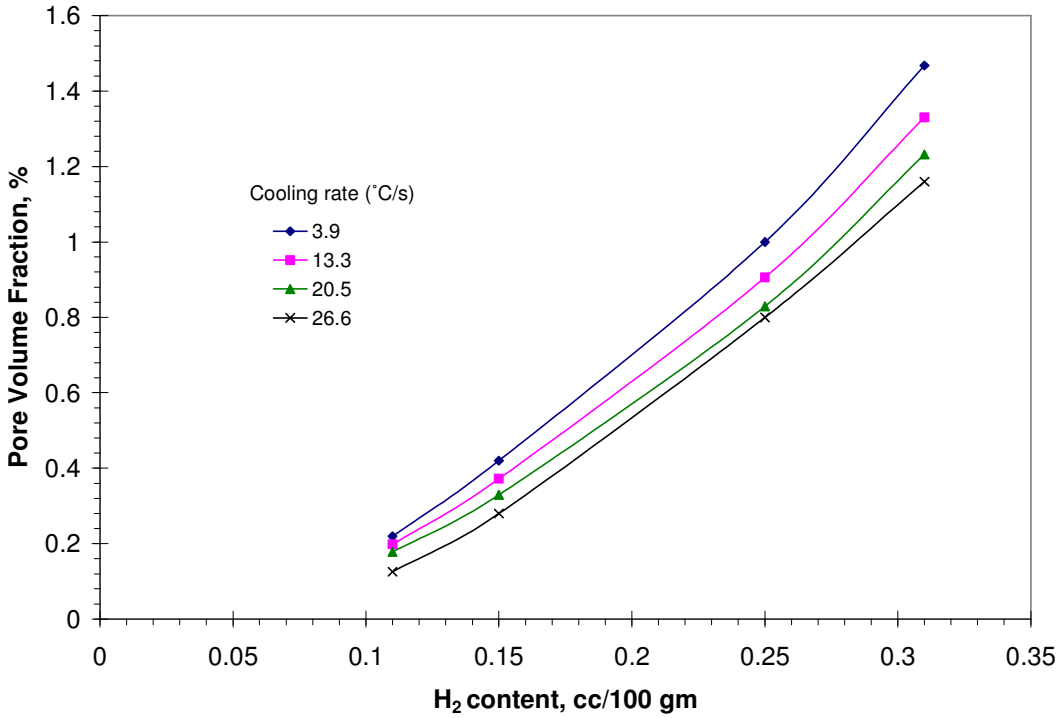

Figure 6.3 Volume fraction of porosity for different cooling rates as a function of initial hydrogen content

6.1.3 Effect of grain size

The simulations above were performed using a final grain diameter of 0.5 mm, which is in the range of values reported by Fang and Granger [3] for the experiments with refined castings. In their study, they observed the effects of grain refining in aluminum castings with an initial hydrogen concentration of 0.25 cc/100g. According to the experimental data, the amount of porosity of non-grain refined castings is higher than that of grain refined in around 20%. To verify whether or not the model could predict values with this trend, we simulate a case of non-refined alloy by using a grain diameter of 3mm. Figure 6.4 shows the

amounts of porosity with 0.25 cc/100g of initial hydrogen content as a function of the cooling rate.

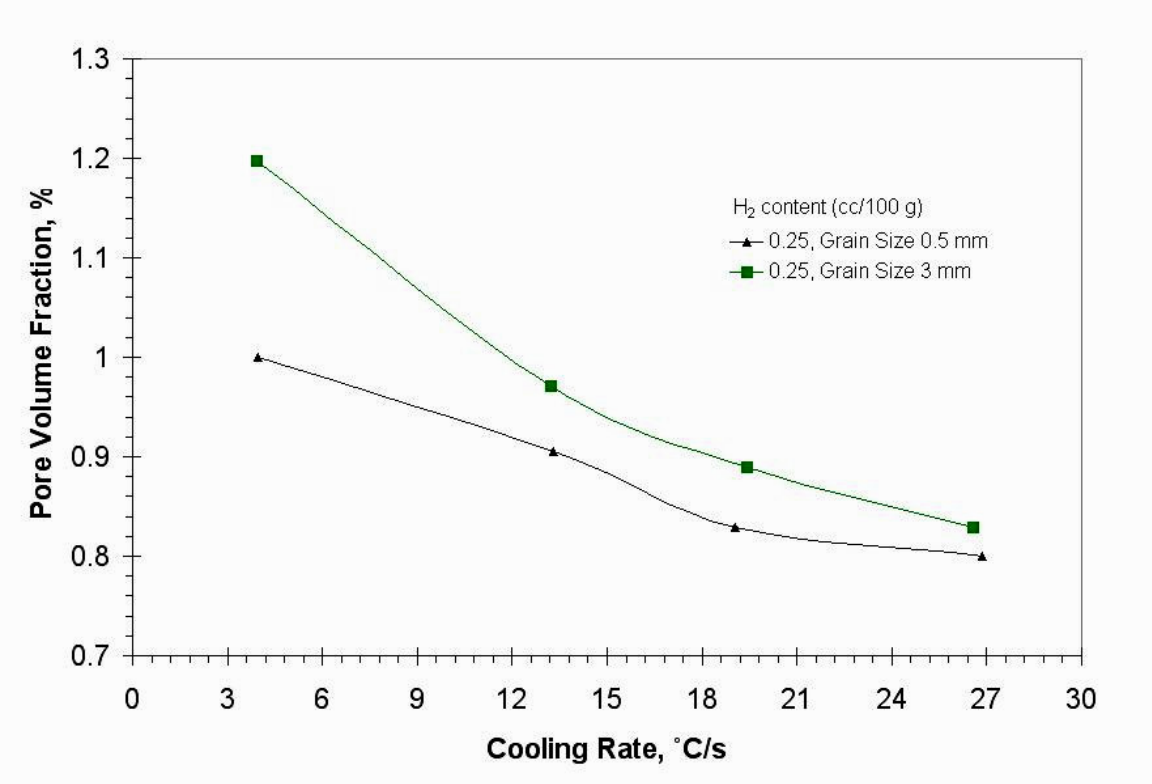

Figure 6.4 Volume fraction of porosity as a function of cooling rate and grain size

In Figure 6.4 it is observed that the alloy with larger grain size presents a higher amount of potential porosity, as reported in the experimental data. For low cooling rates, the increase of porosity is similar quantitatively to that measured in the experiments (about 20%), but the increase becomes very small at high cooling rates. The reason for this behavior is the following: the alloy with coarser grains has larger permeability and stronger convection, leading to higher macrosegregation of hydrogen [7]. The convection dies down at high cooling rate, reducing the macrosegregation of hydrogen and the porosity.

6.2. Method B – Semi-Empirical technique

6.2.1 Comparison of predictions with Fang and Granger [3] experimental data

The purpose of this method is to improve the quantitative prediction of volume fraction of porosity made with the model presented in Method A. The volume fraction of porosity for initial hydrogen contents of 0.11, 0.25 and 0.31 cc/100g is shown in Figure 6.5 (a, b, c). The cooling rate is computed from the temperature history and solidification time calculated in the model as:

$$r = \frac{T_L - T_E}{t_f} \tag{24}$$

where r is the cooling rate, T_E is the eutectic temperature, T_L is the liquidus temperature defined in Eq. (6), and t_f is the time lapsed between T_L and the end of eutectic solidification.

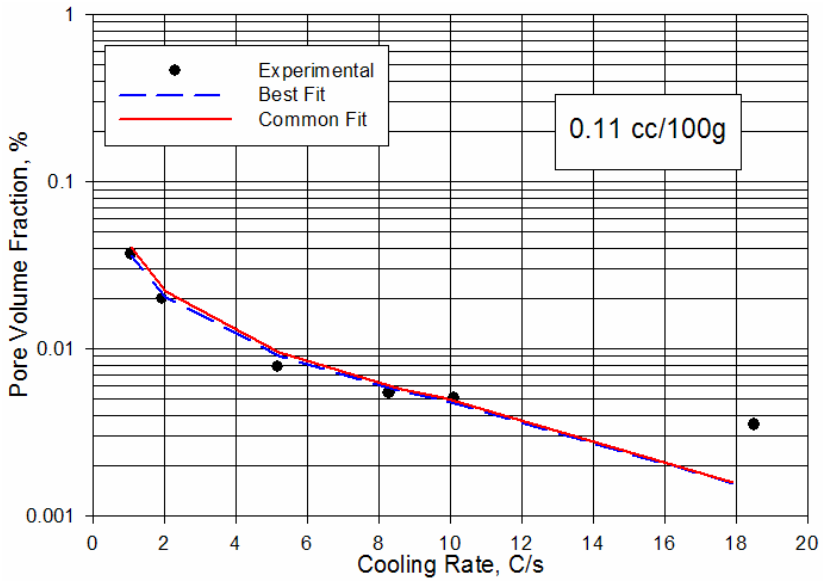

(a)

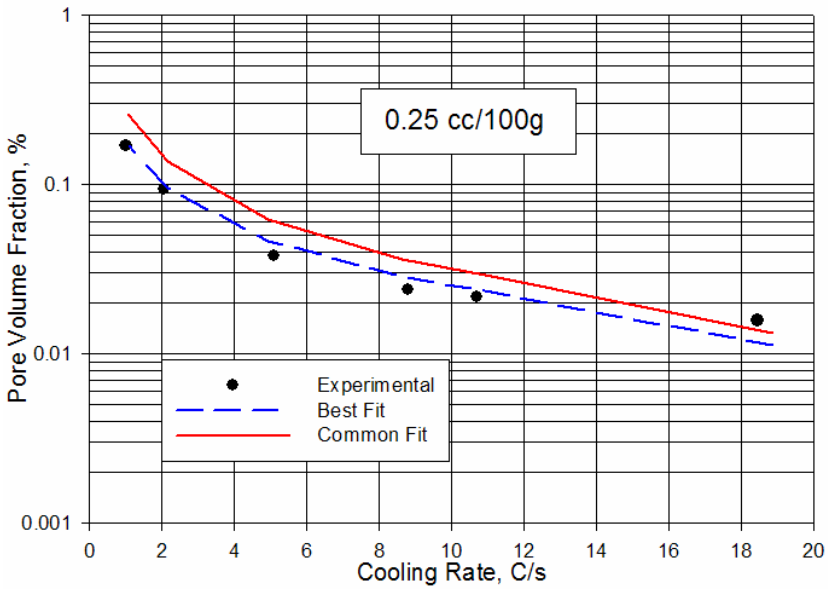

(b)

Figure 6.5 Comparison of experimental [3] and predicted porosity values using empirical method B varying the initial hydrogen content.

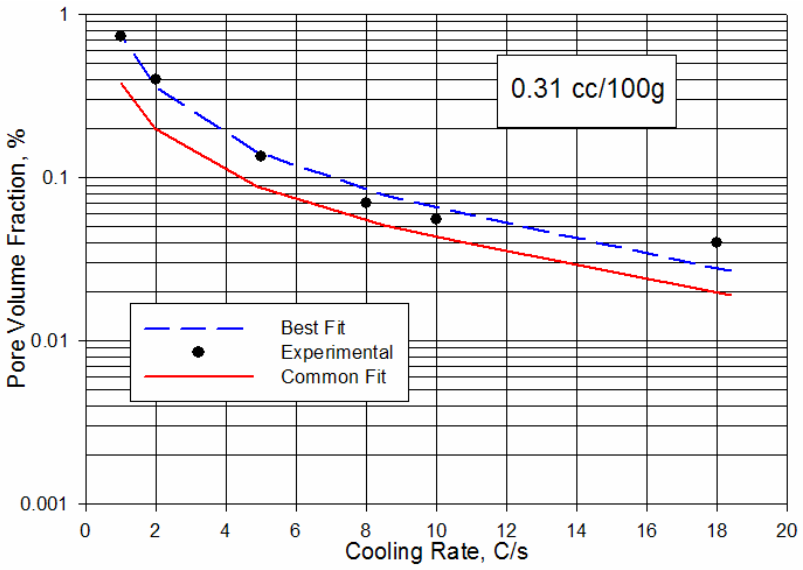

(c)

Figure 6.5 Continued - Comparison of experimental [3] and predicted porosity values using empirical method B varying the initial hydrogen content.

In Figure 6.5, the dashed line labeled “Best Fit “is the porosity calculated with Equation (15), using the best fit of the constants *a* and *b* for a given hydrogen content. Each initial hydrogen content was studied separately, and the values calculated with the least square method of *a* and *b* that fits the experimental data better are presented in Table 6.1.

Table 6.1

Best fit values for constants a and b

	0.11 cc/100 g	0.25 cc/100 g	0.31 cc/100g
a	0.00298	0.00232	0.00318
b	0.93549	0.91713	1.08111

After calculating the values for each initial hydrogen content, a study was carried out to determine the best common fit that will adjust all the curves. The best common fit was obtained with constants a = 0.003 and b = 0.97. It is observed in Figure 6.5 that, when the experimental constants are fit for an individual hydrogen content, the predicted porosity (dashed line) agrees very well with the experimental data (error less than 10%), except at the highest value of cooling rate. For the three values of initial hydrogen content considered, the best fit prediction underestimated the porosity calculated at the highest value of cooling rate. This discrepancy is expected because of the contribution of shrinkage porosity (not considered in these calculations): at a high cooling rate (short freezing time) there is not enough time for the gas pores to evolve and shrinkage porosity becomes relatively more important.

If we proceed to predict the amount of porosity using a common set of constants in Equation (15) for all values of hydrogen content, it is observed (solid lines in Figure 6.5) that the accuracy of prediction is varied, with a good capture of the cooling rate trend but less accuracy in the level of porosity. This might indicate that the number of originated pores is not directly related to the level of hydrogen supersaturation, but they could arise from alternative mechanisms of pore formation like the presence of inclusions or the entrainment of oxide bifilms.

6.2.2 Comparison of predictions with Anyalebechi [36] experimental data

In order to see whether the found values of a and b hold for other experiments, simulations were ran for a different experimental setup of A356. An

experimental setup, similar to the one used by Fang and Granger [3], was presented by Anyalebechi in 2003 [36]. A bench-scale unidirectional cooling casting apparatus was used for the experiments. Anyalebechi presented experimental results of volume percent of porosity as a function of the solidification rate for an aluminum alloy with an initial hydrogen concentration of 0.27 cc/100g (Figure 6.6). The thermal boundary conditions were very similar to the one presented by Fang and Granger [3]. Even when the dimensions of the castings were different, the cooling rate trend, in Figure 6.6, still follows the experimental behavior rather well.

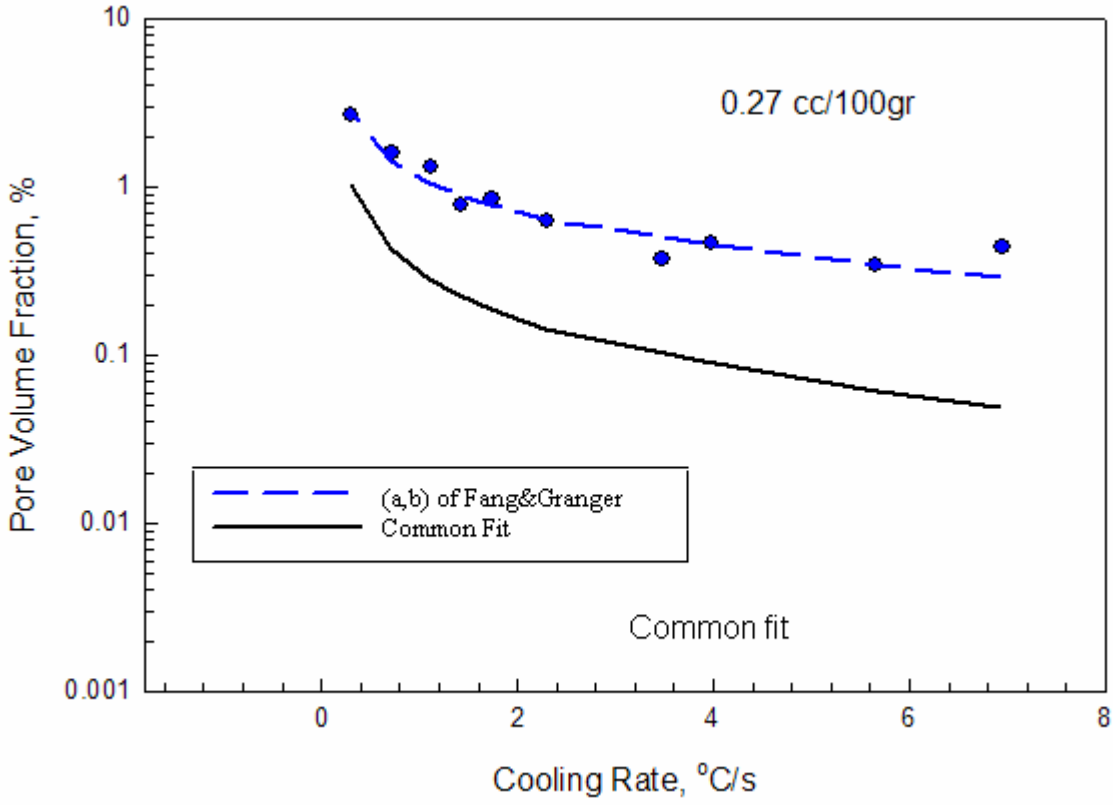

Figure 6.6 Comparison of experimental [36] and predicted porosity values using the best common fit parameters *a* and *b.*

6.3. Method C – Hydrogen diffusion technique

Using the hydrogen diffusion technique, simulations were performed with the same amounts of initial hydrogen contents used for Methods A and B. For all of the calculations presented in this method, it is used an initial pore diameter of 3μm and an inclusion density of $2x10^{11}$ m^{-3}. Taking the density of alumina as 4000 kg/m^3 and spherical inclusion size equal to the initial pore size, this inclusion density corresponds to a concentration of approximately 5 ppm . This selection was guided by the work of Simensen and Berg [39], who found that the smallest alumina particles in aluminum and aluminum alloys ranged from 0.2 to 10 μm, while the concentration of oxides varied between 6 and 16 ppm.

Figures 6.7, 6.8 and 6.9 shows the variation of pore volume fraction and pore diameter versus cooling rate in the solidified casting for all three values of initial hydrogen content. In this figure, the pink dots are calculated values that span of all the casting; each dot represents the pore volume fraction or pore diameter calculated at a mesh node in the casting.

In order to achieve the agreeing results obtained in Figures 6.7, 6.8 and 6.9 neglecting the surface tension term was necessary in the porosity formation condition in Equation (16). This can be explained with the oxide bifilms theory; the bifilms is an air pocket and is considered the originator of a pore [1, 38]. It is interesting to note that if the bifilms theory is correct, then there is not direct contact between gas and liquid and hence no surface tension is involved.

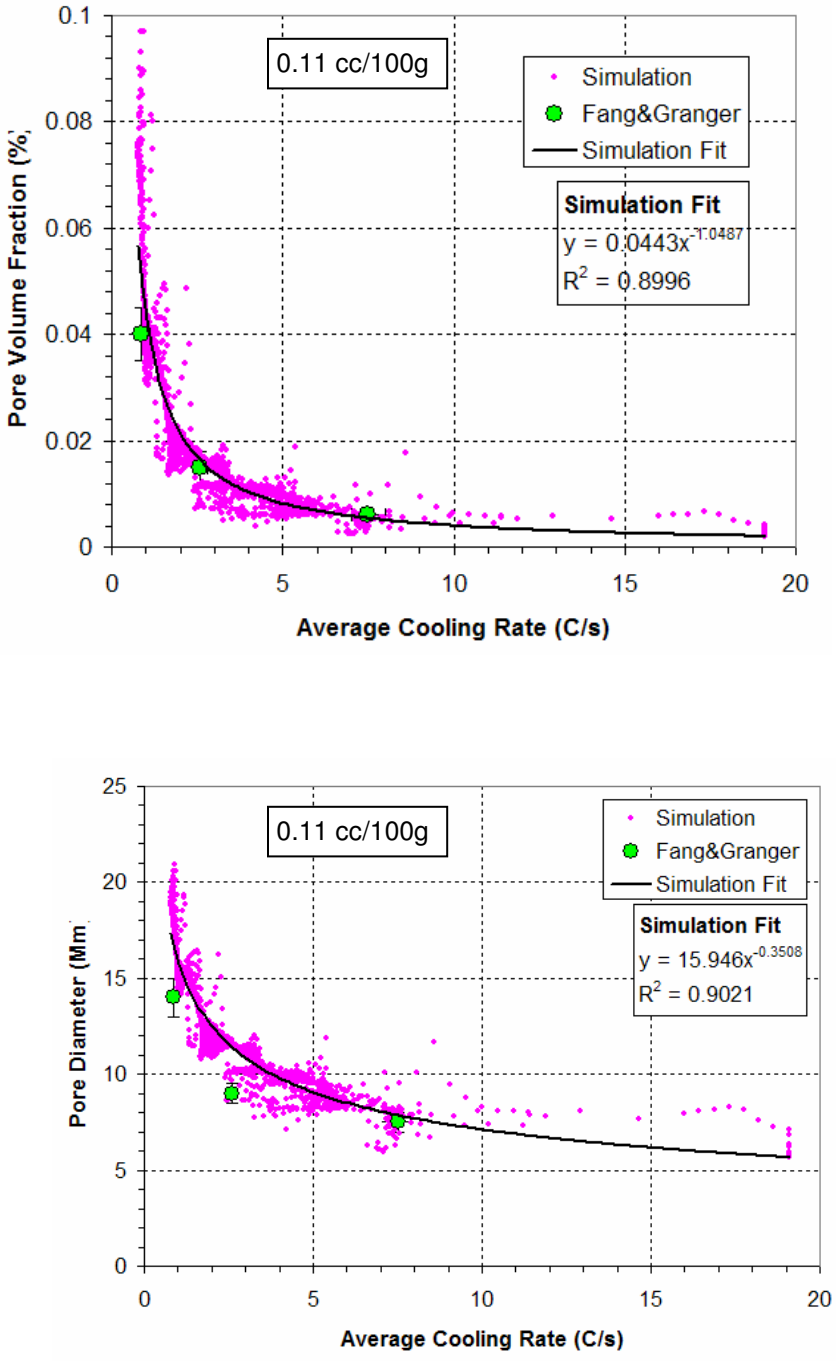

Figure 6.7 Pore volume fractions and pore diameters as a function of cooling rate for an initial hydrogen content of 0.11 cc/100g.

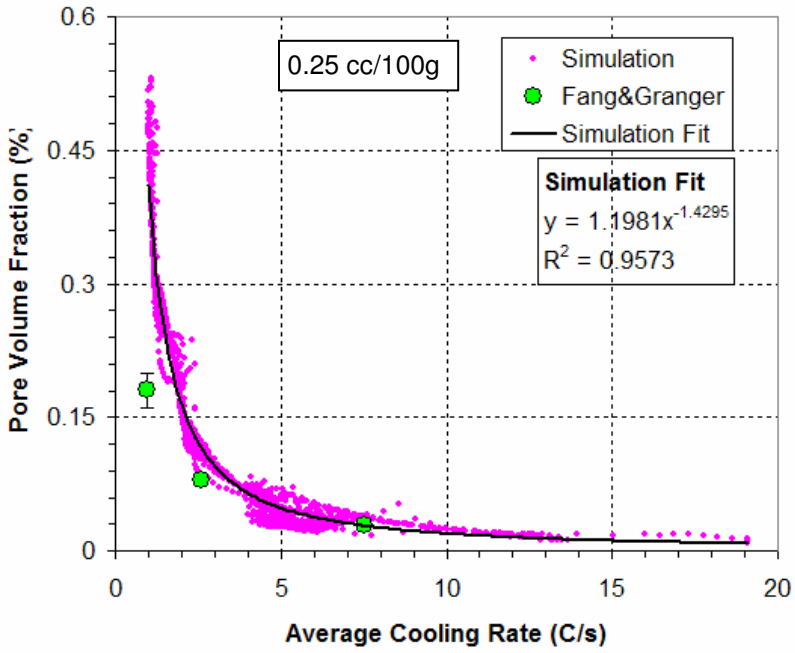

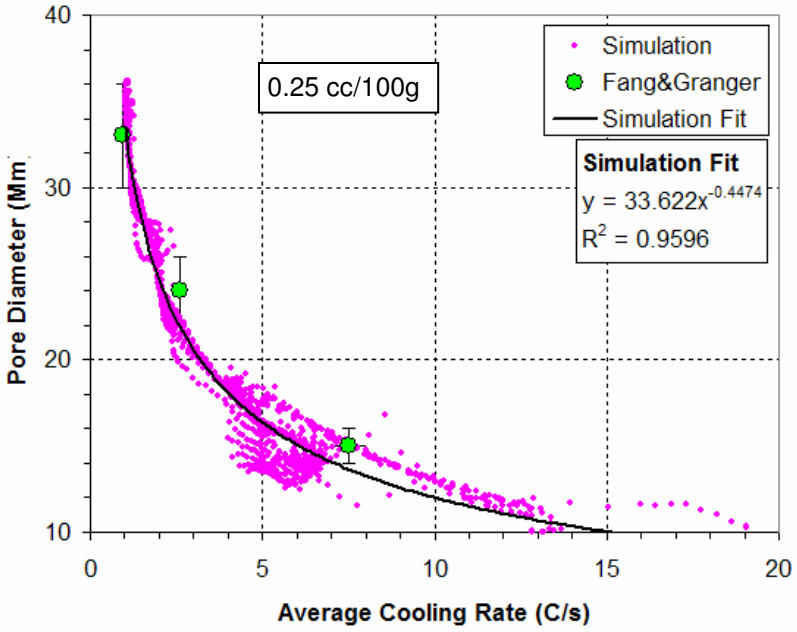

Figure 6.8 Pore volume fractions and pore diameters as a function of cooling rate for an initial hydrogen content of 0.25 cc/100g.

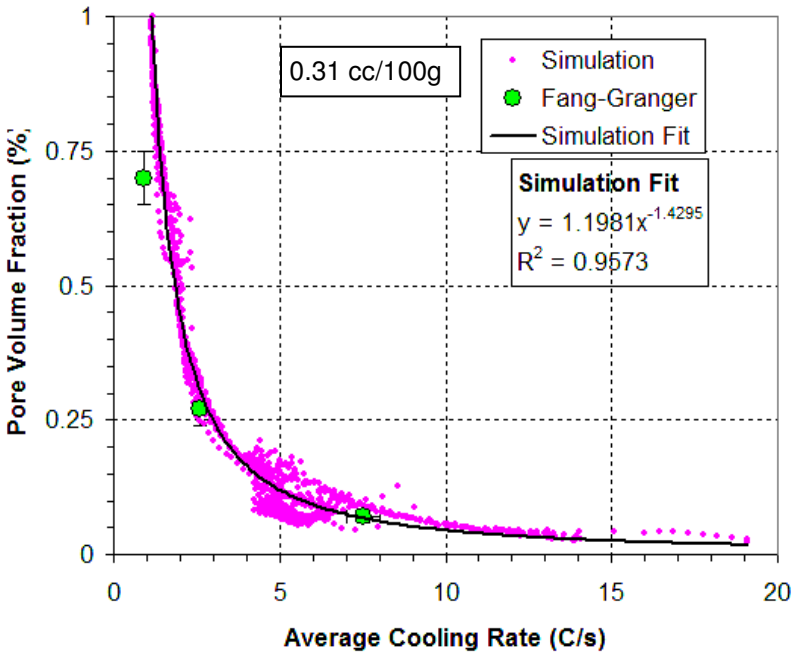

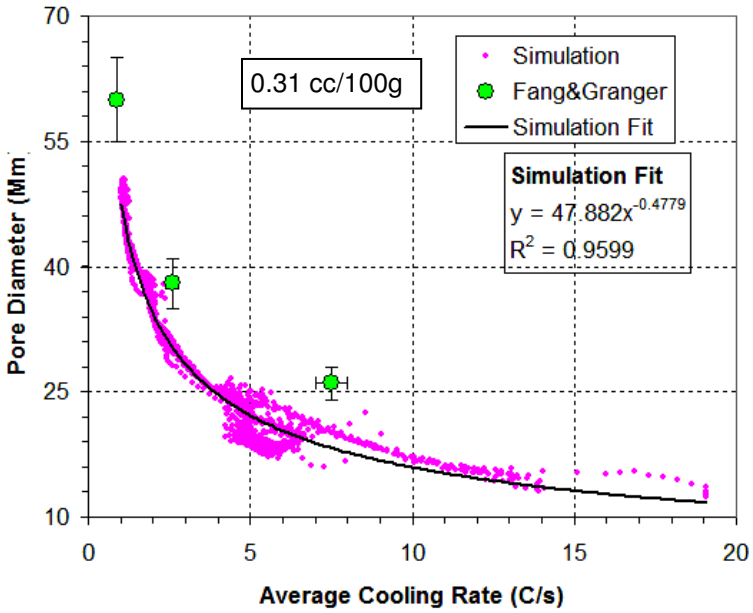

Figure 6.9 Pore volume fractions and pore diameters as a function of cooling rate for an initial hydrogen content of 0.31 cc/100g.

A least square fit of the calculated values is also shown as a solid black line. The experimental data of Fang and Granger [3] are indicated as green dots; this data was taken from their paper; so bars estimating possible reading error are added. The experimental green dots represent average values measured at a certain section of the casting, while the simulation shows the space variation within the entire casting. Certainly, the pore volume fraction and diameter are affected by other solidification variables in addition to the cooling rate, but an average trend can be identified, whereas they both decrease for higher cooling rates.

The quantitative agreement of simulated results with the experimental data is reasonable, considering that it is used a relatively simple two-dimensional continuum model. As previously mentioned, all of the results in Figures 6.7 were obtained using the same values of the initial pore diameter, (d_0 = 3 μm), and concentration of inclusions, (n = 2x10^{11} m^{-3}). Although the selected values fall in the experimentally measured range reported [39], it is possible that pores originate within a range of sizes and that the concentration of inclusions may differ from one casting to another in the experiments of Fang and Granger [3]. A closer agreement with the experimental data can be obtained if the parameters d_0 and n are adjusted individually for each level of hydrogen content, but this approach was not pursued. In this sense, a same set of parameters works rather well for all three castings.

In addition to d_0 and n, a pore shape parameter, α = 1, was used to obtain the results for the castings with 0.25 and 0.31 cc/100g of hydrogen content,

indicating that the growth of pores in these castings apparently was not affected significantly by impingement of the pores on dendrites. However, we needed to use $\alpha = 4$ to reproduce the results of the 0.11 cc/100g casting, probably indicating that in this casting, the pores were distorted significantly during growth. This observation is supported by the calculated fraction of liquid at which pores activate in each casting: 0.45, 0.75 and 0.85, for the 0.11, 0.25 and 0.31 cc/100g castings, respectively. It was observed in the simulations that once activated, pores grew very fast, indicating that in the 0.25 and 0.31 cc/100g castings, the pores developed most of their size at high fraction of liquid and were not affected significantly by dendrite impingement. In contrast, in the 0.11 cc/100g casting, pores started to grow at an already high fraction of solid and were most probably distorted largely by dendrites during growth.

CHAPTER VII

SUMMARY AND CONCLUSIONS

A finite element model of dendritic solidification was extended to allow the calculation of microporosity in aluminum plate castings. Three methods to calculate the amount of porosity assuming different implications were developed, showing in some cases good agreement with experimental data.

A first method, which neglects nucleation and growth effects, was presented. As expected, the quantity of porosity is overpredicted highly. However, even when the values are overpredicted, the model still captures the trends observed in real castings, like the increase of porosity with hydrogen content and with grain size.

A second method, based in a semi-empirical relation on the local solidification time and the fraction of active nucleation sites, was presented. The prediction of the amount of porosity is improved significantly when the effects of nucleation and growth are added. The results obtained with the second method show the importance that pore formation and growth considerations have in for the modeling of aluminum casting solidification.

Finally, a third method, based in a hydrogen diffusion technique, was presented. The pore volume fraction and pore size distribution were calculated,

based on an initial pore size and inclusion concentration. The simulations show that the same set of these parameters is able to reproduce, with reasonable agreement, experimental data from different castings with varying levels of hydrogen content.

Future work would be desirable to implement new approaches to calculate the thickness of diffusion boundary layers for the hydrogen diffusion technique. Also, a micro-model, to study the formation of bifilms and their relation to hydrogen porosity, is necessary; in order to obtain a better understanding of the phenomena that leads to porosity defects in castings.

REFERENCES

[1] Campbell J: *Castings 2nd Edition – The New Metallurgy of Cast Metals*. Butterworth-Heinemann, Oxford, UK, 2003

[2] Felicelli S D, Poirier D R and Sung P K: A model for prediction of pressure and redistribution of gas- forming elements in multicomponent casting alloys, *Metall. Mater. Trans. B* Vol. 31B (2000), 1283-1292

[3] Fang Q T and Granger D A: Porosity formation in modified and unmodified A356 alloy castings, *AFS Trans.* Vol. 97 (1989), 989-1000

[4] Han Q and Viswanathan S: Hydrogen evolution during directional solidifications and its effect on porosity formation in aluminum alloys, *Metall. Mater. Trans. A* Vol. 33A (2002), 2067-2072

[5] Lee P D and Hunt J D: Hydrogen porosity in directional solidified aluminum-copper alloys: a mathematical model, *Acta Mater.* Vol. 49 (2001), 1383-1398

[6] M'Hamdi M, Magnusson T, Pequet Ch, Arnberg L and Rappaz M: Modeling of microporosity formation during directional solidification of an Al-7%Si alloy, *Modeling of Casting, Welding and Advanced Solidification Processes X*, D.M. Stefanescu, J. Warren, M. Jolly, and M. Krane (Eds.), The Minerals, Metals, & Materials Society, 2003, 311-318

[7] Poirier D R, Sung P K and Felicelli S D: A continuum model of microporosity in an aluminum casting alloy, *AFS Trans.* Vol. 109 (2001), 379-395

[8] Zhu J D, Cockcroft S L, Maijer D M and Ding R: Simulation of microporosity in A356 aluminium alloy castings, *Int. J. Cast Met. Res.* Vol. 18 (2005), 229-235

[9] Guo J and Samonds M T: Microporosity simulations in multicomponent alloy castings, *Modeling of Casting, Welding and Advanced Solidification*

Processes X, D.M. Stefanescu, J. Warren, M. Jolly, and M. Krane (Eds.), The Minerals, Metals, & Materials Society, 2003, 303-311

[10] Carlson K D, Zhiping L, Hardin R A and Beckermann C: Modeling of porosity formation and feeding flow in steel casting *Modeling of Casting, Welding and Advanced Solidification Processes X*, D.M. Stefanescu, J. Warren, M. Jolly, and M. Krane (Eds.), The Minerals, Metals, & Materials Society, 2003, 295-302

[11] Sung, P K, Poirier D R and Felicelli S D: Continuum model for predicting microporosity in steel castings, *Modelling Simul. Mater. Sci. Eng.* Vol. 10 (2002), 551-568

[12] Sabau A S and Viswanathan S: Microporosity prediction in aluminum alloy castings, *Metall. Mat. Trans. B* Vol. 33B (2002), 243-255

[13] Lee P D, Chirazi A, Atwood R C and Wang W: Multiscale modeling of solidification microstructures, including microsegregation and microporosity, in an Al-Si-Cu alloy, *Mater. Sci. Eng. A* Vol. A365 (2004), 57-65

[14] Yang X, Huang X, Dai X, Campbell J and Tatler J: Numerical modeling of entrainment of oxide film defects in filling of aluminium alloy castings, *Int. J. Cast Met. Res* Vol. 17 (2004), 321-331

[15] Stefanescu D M: Computer simulation of shrinkage related defects in metal castings – a review. *Int. J. Cast Met. Res.* Vol. 18 (2005), 129-143

[16] Felicelli S D, Heinrich J C and Poirier D R: Finite element analysis of directional solidification of multicomponent alloys, *Int. J. Numer. Meth. Fluids* Vol. 27 (1998), 207-27

[17] Escobar E and Felicelli S D, Quantitative prediction of microporosity in aluminum alloys *Journal of Materials Processing Technology,* in press (2006)

[18] S.D. Felicelli, E. Escobar de Obaldia, C.M. Pita, Simulation of hydrogen porosity during solidification, accepted in *AFS Transactions* (2006).

[19] S.D. Felicelli and E. Escobar de Obaldia, Nucleation and growth effects in the accuracy of predicted gas porosity during solidification of A356 aluminum alloys, accepted in *Journal of Numerical Analysis, Industrial and Applied Mathematics* (2006)

[20] S.D.Felicelli, C. Pita and E. Escobar de Obaldia, Modeling the onset and evolution of hydrogen pores during solidification, *Shape Casting:2nd International Symposium Edited by Paul N. Crepau, Murat Tiryakioglu and John Campbell,* TMS, pp 201-208 (2006)

[21] E. Escobar de Obaldia and S.D. Felicelli, Numerical modeling of microporosity during solidification, *ICNAAM – International Conference on Numerical Analysis and Applied Mathematics 2006*, T.E. Simos, G. Psihoyios, Ch. Tsitouras, edts., Wiley-VCH Verlag, pp. 105-108, 2006

[22] Felicelli S D and Escobar E, Numerical simulation of hydrogen microporosity in aluminum castings, *Conference of Advances in Materials and Processing Technologies*, AMPT, Las Vegas – Nevada. August 2006.

[23] Piwonka T S, Flemings M C: Pore formation in solidification, *Trans. AIME,* v 236, 1966, 1157-1165

[24] Flemings M C: Solidification modeling, Past and Present, *Modeling of Casting, Welding and Advanced Solidification Processes,* v III, ed. B.G. Thomas and C. Beckermann, (1998), 1-13

[25] Flemings M C, Nereo G E: Macrosegregation: Part I, Trans, AIME, 239, (1967), 1449 – 1461

[26] Flemings M C 1974 *Solidification Processing* (New York: McGraw-Hill) pp 203-10

[27] Taylor R P, Berry J T and Overfelt R A *Parallel Derivation and Comparison of Feeding Resistance Porosity Criteria Functions for Castings,* ASME 1996 Natl. Heat Transfer Conference, Vol 323, pp 69 - 77

[28] Lee P D, Hunt J D: Hydrogen porosity in directional solidified aluminum-copper alloys: in situ observation, *Acta Mater.*, v 45, n 10, 1997, p 4155-4169

[29] Niyama E, Uchida T, Morikawa M and Saito S, Predicting Shrinkage in Large Steel Castings from Temperature Gradient Calculations, *AFS International Cast Metals Journal,* June 1981, p 17.

[30] Felicelli S D, Poirier D R and Heinrich J C 1998b Modeling freckle formation in three dimensions during solidification of multicomponent alloys *Metall. Mater. Trans. B* 29B 847-855

[31] Bhat M S 1995 *Ph.D. Dissertation*, The University of Arizona, Tucson, AZ

[32] Anyalebechi P N 1995 Analysis of the Effects of Alloying Elements on Hydrogen Solubility in Liquid Aluminum Alloys *Scripta Metall. Mater.* 33 1209 1216

[33] Anyalebechi P N 1998 Analysis and Thermodynamic Prediction of Hydrogen Solution in Solid and Liquid Multicomponent Aluminum Alloys *Light Metal 1998*, Welch B (ed.), TMS, Warrendale, PA, pp 827-842

[34] Poirier D R and Sung P K 2002 Thermodynamics of hydrogen in Al-Si alloys *Met. Mater. Trans. A* 33A 3874-3876

[35] Poirier D R, Yeum K, and Maples A L 1987 A thermodynamic prediction for microporosity formation in aluminum-rich Al-Cu alloys *Metall. Mater. Trans. A* 18A 1979-1987

[36] Anyalebechi P N Effects of hydrogen, solidification rate, and Ca on porosity formation in as-cast aluminum alloy A356, *Light Metals 2003*, P. N. Crepeau (ed.), TMS, Warrendale, PA, 971-981

[37] Yin H. and Koster J., "In-situ observed pore formation during solidification of aluminium", *ISIJ International*, vol. 40(4), pp. 364-372 (2000)

[38] Campbell J: Entrainment Defects, *Materials Science and Technology* Vol. 22, n 2, (2006), pp 127-145]

[39] Simensen C J and Berg G, A survey of inclusions in aluminum, *Aluminium*, Vol. 56, No. 5, pp. 335-340 (1980)